Iron-Histidine Coordination in Cytochrome b5: A Local Vibrational Mode Study

Marek Freindorf[+],[a] Kevin Fleming,[a] and Elfi Kraka[+]*[a]

For a series of cytochrome b5 proteins isolated from various species, including bacteria, animals, and humans, we analyzed the intrinsic strength of their distal/proximal FeN bonds and the intrinsic stiffness of their axial NFeN bond angles. To assess intrinsic bond strength and bond angle stiffness, we employed local vibrational stretching force constants k^a(FeN) and bending force constants k^a(NFeN) derived from the local mode theory developed by our group; the ferric and ferrous oxidation states of the heme Fe were considered. All calculations were conducted with the QM/MM methodology. We found that the reduction of the heme Fe from the ferric to the ferrous state makes the FeN axial bonds weaker, longer, less covalent, and less polar. Additionally, the axial NFeN bond angle becomes stiffer and less flexible. Local mode force constants turned out to be far more sensitive to the protein environment than geometries; evaluating force constant trends across diverse protein groups and monitoring changes in the axial heme-framework revealed redox-induced changes to the primary coordination sphere of the protein. These results indicate that local mode force constants can serve as useful feature data for training machine learning models that predict cytochrome b5 redox potentials, which currently rely more on geometric data and qualitative descriptors of the protein environment. The insights gained through our investigation also offer valuable guidance for strategically fine-tuning artificial cytochrome b5 proteins and designing new, versatile variants.

Introduction

Electron transfer (ET) is essential for fundamental biochemical processes.[17] Metalloproteins are a class of ET-mediating proteins, and they can be synthetically modified to tune their redox potentials, which in turn influence the kinetics of the ET reactions that they are involved in.[18–24] The synthetic tunability of the proteins' redox potentials also makes them of interest in the field of bioelectrocatalysis,[25] where they are used in the development of biosensors,[26,27] biofuel cells,[28] and artificial metalloenzymes which have catalytic rates rivaling those of native enzymes.[29]

Cytochrome b5 (Cb5) is a heme-containing metalloprotein belonging to the class of hexacoordinated hemoproteins where both the distal and proximal histidine are coordinated to the central Fe atom, which can be in the ferric (Fe(III)) or ferrous (Fe(II)) oxidation states.[30–39] Found in bacteria, fungi, animals, humans, and plants, Cb5 acts an ET mediator[40] in many biochemical reactions such as fatty acid desaturation and elongation,[41,42] cholesterol biosynthesis,[43] and methemoglobin reduction.[44] Cb5 consists of a hydrophilic head domain involving the heme group, and a hydrophobic tail connecting the protein to the microsomal membrane. The standard redox potential for the Fe(III/II) couple is $+0.77$ mV in acidic aqueous

solution versus normal hydrogen electrode (NHE);[45] thus, Fe(III) is spontaneously reduced to Fe(II). In the Cb5 protein, however, the Fe(III/II) redox potential can vary by nearly 400 mV due to the protein's interactions with other redox-active species, surface charge changes, changes to the hydrogen bonding network of the protein backbone, site-directed mutagenesis, and changes to conditions of the surrounding protein environment (i.e, pH, temperature, and ionic strength).[11,46–51] This large set of influencing factors greatly complicates the computational evaluation of Cb5's Fe(III/II) redox potential.

In the past two decades, efforts have been made to calculate redox potentials for large chemical systems using MD,[52] DFT-MD,[53] and QM/MM.[54,55] Recently, machine learning (ML) approaches to evaluating redox potentials have also been proposed in the literature; these models are generally trained on feature data which reflect a given chemical system's geometric structure (i.e., internal coordinate data of optimized/experimental structures), electronic/bonding properties (i.e., bond order, charge/spin distribution, hybridization, dipole moment, electronegativity, orbital energies, and SCF energies), and the surrounding chemical environment.[56–60] These ML models can be further refined during training by providing precise, continuous descriptors of chemical bonding in lieu of imprecise, discrete descriptors (i.e., Lewis bond order). Local vibrational mode analysis (LMA), developed in our group,[61,62] provides precise bond strength and bond angle stiffness information based on vibrational spectroscopy data. By training ML models using datasets that include these holistic second order properties, which are sensitive to both the geometric and electronic structure of a given system, the models may provide more accurate and precise predictions of redox potentials, especially when applied to ET-mediating proteins like Cb5.

[a]   Prof. Dr. M. Freindorf,[+] K. Fleming, Prof. Dr. E. Kraka[+]
      Computational and Theoretical Chemistry Group (CATCO), Department of
      Chemistry, Southern Methodist University, 3215 Daniel Ave, Dallas, TX
      75275-0314, USA
      E-mail: ekraka@smu.edu
[+]   These authors contributed equally.

⌨   Supporting information for this article is available on the WWW under
      https://doi.org/10.1002/cphc.202401098

ChemPhysChem

Research Article
doi.org/10.1002/cphc.202401098

Chemistry Europe
European Chemical
Societies Publishing

Changes to both the electronic and geometric structure of Cb5's primary coordination sphere occur during the reduction of the central heme Fe from the ferric state to the ferrous state. Redox-induced changes to the length and strength of axial bonds between the heme iron and the coordinated histidine ligands (i.e., FeN bonds), as well as changes involving the relative orientation and flexibility of these two ligands (i.e., NFeN bond angle), can be indicative of the relative stability of the ferric and ferrous states of the heme iron. The relative stability of these two states, in turn, may be related to the redox potential of the protein, as observed in the case of heme-containing peroxidases.[63] In addition, theoretical and experimental studies have shown that the properties of bis-histidyl-ligated hemoproteins depend on the axial Fe-histidine linkage and that different orientations of the histidine imidazole planes with respect to the heme framework can shift the heme redox potential.[64–68] Therefore, accounting for FeN bond strength and NFeN bond angle stiffness data obtained via LMA when training ML models may lead to more precise and accurate predictions of the potentials of Cb5/Cb5-like proteins, thereby better facilitating the design of engineered proteins whose potentials would be precisely fine-tuned for the use of these proteins in important bioelectrocatalytic technologies.

Inspired by this promising application, we utilized LMA in this study to examine redox-induced changes to axial FeN bond strengths and axial NFeN bond angle stiffnesses in a series of Cb5s presented in Table 1. This list is based on available X-ray structures of Cb5s originating from the green alga virus (**ALG**), a bacterium (**BCB**), archaeon (**BCC**), cattle (**BOM** and **BOV**), chicken (**CHK**), house fly (**FLY**), human (**HUM**), pig (**PIG**), rat (**RAT**), water bear (**WBR**), and the large roundworm of pig (**WRM**). Differences between the structures' primary coordination spheres (i.e., FeN bond lengths and NFeN bond angles) may occur partly due to differences in their secondary coordination spheres, as previously observed in an infrared multiple photon dissociation spectroscopy study of various conformers of a Fe(III) protoporphyrin IX complex with an imidazole axial ligand.[69] The structures also vary significantly in terms of their experimentally determined redox potentials, as shown in Table 1. The X-ray structure of the green alga virus Cb5 (**ALG**) from *Ostreococcus tauri virus 2* was reported at a resolution of 1.95 Å[1] and shows similarity to those found in larger eukaryotic cytochrome proteins. However, **ALG** lacks a hydrophobic C-terminal anchor, which is required for membrane attachment in contrast to other microsomal Cb5s. The X-ray structure of the bacterium Cb5 (**BCB**) from *Ectothiorhodospira vacuolata* was reported at a resolution of 1.65 Å.[2] It represents cytochrome b558, which is a prokaryotic homologue of Cb5. The X-ray structure of **BCB** was the first bacterial cytochrome b5 to be analyzed, and it differs from other Cb5s by the presence of a disulfide bridge and a unique arrangement in front of the distal histidine. The archaeon Cb5 investigated in this study (**BCC**) is from *Methanococcoides burtonii*. The X-ray structure of **BCC** was reported at a resolution of 2.1 Å.[3] **BCC** is an Cb5 M protein related to a membrane-associated progesterone receptor and shows a specific orientation of the heme group, which is strongly rotated relative to other Cb5s. The X-ray structure of the cattle Cb5 (**BOM**) from *Bos taurus* corresponds to a Phe35Tyr protein mutation, reported at a resolution of 1.8 Å.[4] Phenylalanine 35 has a hydrophobic side chain on the Cb5 surface and is in direct Van der Waals contact with the heme group. The Phe35Tyr mutation introduces interactions between the side chain of Tyr35 and the heme group, resulting in increased stability of the mutant. The X-ray structure of wild-type cattle Cb5 (**BOV**) from *Bos taurus* was reported at a resolution of 1.5 Å.[6] The high-resolution structure confirmed that the ability of Cb5 to form complexes with different electron-transfer proteins is due to the high flexibility of surface polar residues, while the polypeptide backbone remains relatively unchanged. The X-ray structure of chicken liver sulfite oxidase ((**CHK**) from *Gallus gallus domesticus* was reported at a resolution of 1.9 Å.[7] It shows that each monomer of this dimeric enzyme consists of three domains, one of which involves Cb5. The N-terminal domain of CHK resembles bovine cytochrome b5 and consists of three β-sheets and α-helices. The X-ray structure of Cb5 isolated from the housefly, *Musca*

Table 1. Labels, PDB entries, scientific source names, common source names, and previously reported redox potentials, if available, for the twelve Cb5 structures investigated in this study.

Label	PDB entry	Scientific name	Common name	Redox Potential (mV)	Ref.
ALG	4B8N	*Ostreococcus tauri virus 2*	Green alga virus	–	[1]
BCB	1CXY	*Ectothiorhodospira vacuolata*	Bacterium	–	[2]
BCC	6VZ6	*Methanococcoides burtonii*	Archaeon	–	[3]
BOM	1M20	*Bos taurus*	Cattle	−1	[4,5]
BOV	1CYO	*Bos taurus*	Cattle	−66	[5,6]
CHK	1SOX	*Gallus gallus domesticus*	Chicken	–	[7]
FLY	2IBJ	*Musca domestica*	House fly	−26	[8,9]
HUM	3NER	*Homo sapiens*	Human	−2.6	[10,11]
PIG	3X32	*Sus scrofa domesticus*	Pig	–	[12]
RAT	1ICC	*Rattus norvegicus*	Rat	−102	[13,14]
WBR	7BWH	*Ramazzottius varieornatus*	Water bear	–	[15]
WRM	1X3X	*Ascaris suum*	Large roundworm of pig	+75	[16]

domestica, **FLY**, was reported at a resolution of 1.55 Å.[8] The Cb5 **FLY** has an extended hydrophobic region, including a bulky side chain at the base of the heme pocket. Additionally, one α-helix differs substantially in length and packing arrangements compared to Cb5 from other protein isoforms, providing greater stability through hydrophobic interactions. The X-ray structure of human Cb5 (**HUM**) from *Homo sapiens* was reported at a resolution of 1.45 Å.[10] **HUM** is a mammalian type B Cb5 and shows a significant difference in the packing arrangement of its five-strand β-sheet relative to rat type B Cb5. Although **HUM** allows much greater access of water to the protein interior than rat Cb5, both proteins exhibit very similar stability, dynamics, and redox properties. The pig Cb5 **PIG** from *Sus scrofa domesticus* was analyzed, based on its X-ray structure, reported at a high resolution of 0.83 Å.[12] The heme coordination in **PIG** is arranged similarly in both its oxidized and reduced states. However, structural differences are observed between the oxidized and reduced forms in the hydrogen-bond network involving the proximal histidine. The X-ray structure of rat Cb5 (**RAT**) from *Rattus norvegicus* was reported at a resolution of 2.0 Å.[13] It represents the outer mitochondrial membrane isoform of Cb5. NMR spectroscopy and X-ray structure analyses of (**RAT**), compared with bovine microsomal Cb5 and rat mitochondrial Cb5 mutations, indicated that a residue at position 32 is responsible for the relative stability of the heme group in **RAT**. The final two Cb5 proteins investigated in this study are water bear Cb5 (**WBR**) from *Ramazzottius varieornatus* and the large roundworm of pig Cb5 (**WRM**) from *Ascaris suum*. The X-ray structure of **WBR** was reported at a resolution of 1.4 Å,[15] and represents the Cb5 structure of a microscopic multicellular organism (tardigrade) that thrives under extreme conditions in diverse environments such as high mountains and the deep sea. Although amino acid sequences of Cb5 proteins are generally well-conserved, **WBR** is a unique protein with relatively low similarity to the amino acid sequences of other Cb5s, making it responsible for biological processes specific to tardigrades. The X-ray structure of **WRM** was reported at a resolution of 1.8 Å[16] and reveals a unique Cb5 structure that includes an additional α-helix and positively charged residues on the surface for interactions with redox partners. **WRM** also differs from its mammalian counterparts by possessing a disulfide bridge that links the head and tail of the protein. The axial bishistidyl FeN linkage present in all twelve Cb5s is depicted in Figure 1.

Methodology and Computational Details

LMA provides a detailed, bond-specific understanding of vibrational properties by analyzing local vibrational modes rather than normal vibrational modes, which are generally delocalized in polyatomic molecules.[70–73] As such, the use of normal vibrational force constants (derived from a normal mode analysis[70]) as a bond strength measure is limited. Our local vibrational mode analysis,[61,62] originally developed by Konkoli and Cremer,[74,75] has solved this problem via extracting local vibrational modes and corresponding local mode force constant from the normal vibrational modes.
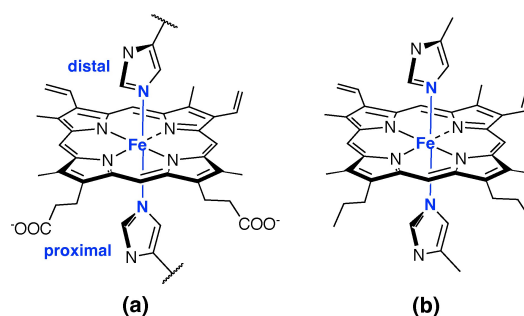

Figure 1. Sketch of the cytochrome b5 axial bishistidyl FeN linkage shown in blue color. **(a)** QM part of the cytochrome b5 active site; **(b)** Gas phase model.

A local vibrational mode $\mathbf{a}_n$ is defined as:

$$\mathbf{a}_n = \frac{\mathbf{K}^{-1}\mathbf{d}_n^\dagger}{\mathbf{d}_n\mathbf{K}^{-1}\mathbf{d}_n^\dagger} \qquad (1)$$

The two ingredients needed for LMA, the diagonal normal mode force constant matrix $\mathbf{K}$ in normal mode coordinates $\mathbf{Q}$ and the normal mode vectors $\mathbf{d}_n$ in internal coordinates, can be obtained from a vibrational frequency calculation via the Wilson GF formalism,[72,73] which is a routine part of most modern quantum chemistry packages.[76] As a consequence, LMA can be applied with minimal computational costs after a routine quantum-chemical calculation of vibrational frequencies, optionally adding measured frequencies as input (a feature which makes LMA accessible to experimental vibrational spectroscopists), to examine either single molecules (in gas phase, solution, or in a protein environment) or periodic/crystalline systems.[61,62]

For each local mode $\mathbf{a}_n$, one can derive associated local force constants k_n^a describing the local vibration of the atomic fragment under consideration,

$$k_n^a = \mathbf{a}_n^\dagger\mathbf{K}\mathbf{a}_n = \frac{1}{\mathbf{d}_n\mathbf{K}^{-1}\mathbf{d}_n^\dagger} \qquad (2)$$

local mode frequencies, local mode infrared intensities, and other local properties can be determined.[62,77]

Over the past two decades, we have successfully applied local mode force constants to characterize the strength of covalent bonds and non-covalent interactions across the periodic table as documented in two recent review articles[61,62] including bonding inside the active sites of hemoproteins,[78–85] as described below. Another important feature of LMA is the characterization of normal mode (CNM) procedure, which decomposes each normal vibrational mode into local mode contributions.[61,62,86,87] CNM has advanced the interpretation of vibrational spectra to the next level (e.g., identifying which molecular fragments couple in DNA-base pairs or assessing the quality of Stark effect probes with a local probe bond).[81,88–90] A detailed description of the underlying local vibrational mode theory has been discussed in our previous work.[61,62]

In recent years, our group has investigated a variety of hemoproteins (see Figure 2), focusing on the strength of chemical bonds formed between the metal atom of the heme group and various molecular ligands on the distal side of the heme pocket, as well as hydrogen bonds between the ligands and distal residues. Figure 2a
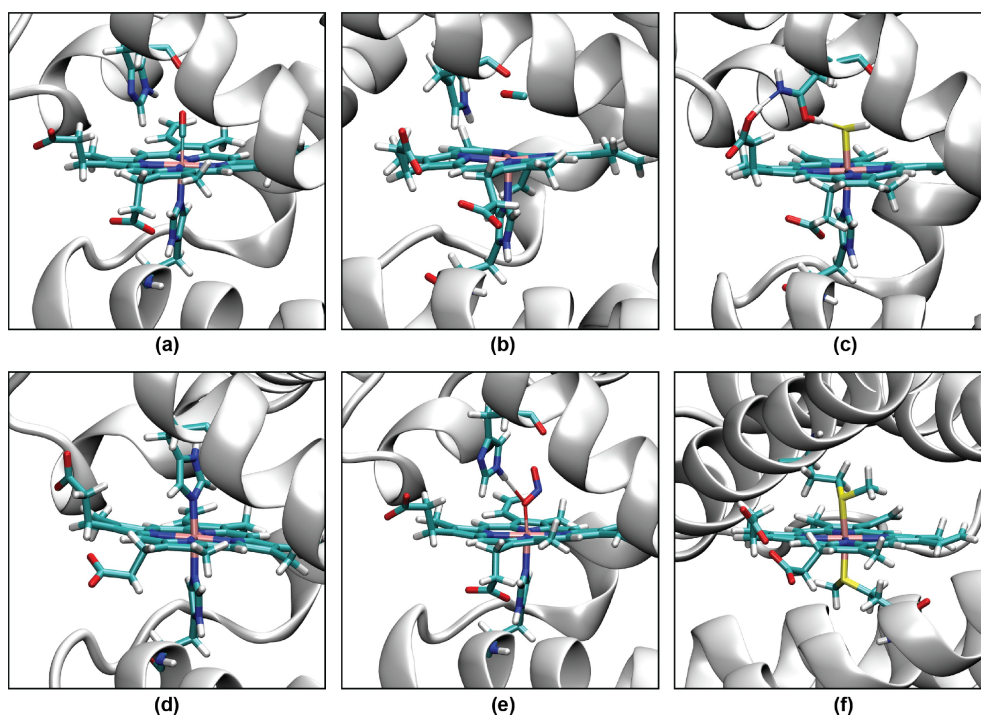
Figure 2. Active sites of hemoproteins investigated in our group; **(a)** myoglobin with CO;[78] **(b)** neuroglobin with CO;[79] **(c)** hemoglobin with H_2S;[83] **(d)** bishistidyl hemoglobin;[84] **(e)** myoglobin with ONO^-; **(f)** bismethionine hemoglobin. For details see the text.

shows the active site of wild-type sperm whale myoglobin with CO coordinated to the heme group (MbCO), which was studied along with 17 protein mutations.[78] In that work, we presented a quantitative measure of the FeC and CO bond strengths in MbCO, as well as of the non-classical hydrogen bonding involving CO⋯H. Figure 2b illustrates an experimentally observed process,[91] in which CO dissociates from the heme group of murine neuroglobin (NgCO) and remains in a docking site within the heme pocket. Inspired by this effect, we analyzed the strength of interactions between the dissociated CO and the heme group, as well as between CO and the surrounding amino acids in the docking site, for wild-type NgCO and its nine mutations.[79] There is a clam living in a sulfur-rich environment,[92] with the active site of hemoglobin occupied by H_2S (see Figure 2c). We also investigated the strength of chemical bonds formed between Fe and H_2S in the wild-type protein and its nine mutations.[83] Our analysis of the wild-type protein revealed a double proton transfer occurring between H_2S and the distal residue of the heme pocket, as well as between the distal residue and one of the propionate groups of the heme. Figure 2d shows the active site of shark hemoglobin, an example of bishistidyl coordination in the heme group. In that study, we investigated the strength of the distal and proximal FeN bonds and the stiffness of the NFeN bond angle in both ferric and ferrous oxidation states of bishistidyl hemoproteins from bacteria, animals, humans, and plants.[84] Figures 2e and 2f show two ongoing projects. The first (Figure 2e) focuses on analyzing the strength of chemical bonds between Fe, Mn, and Co of the heme group in modified myoglobin, and selected molecular ligands such as methanol, water, nitrite, and azide. In this project, we also analyze the strength of hydrogen bonds formed between the ligands and the distal histidine of myoglobin. The second project (illustrated in Figure 2f) examines the strength of FeS chemical bonds on both the distal and proximal sides of bismethionine hemoglobin from bacterioferritin in both oxidation states of Fe.

In this work, we evaluated the force constant $k^a(AB)$, which reflects the intrinsic strength of the bond/weak interaction between two atoms A and B,[93] for the four axial FeN bonds labeled as $Fe_{III}N_{dist}$, $Fe_{III}N_{prox}$, $Fe_{II}N_{dist}$, and $Fe_{II}N_{prox}$, where *dist* and *prox* indicate the distal and proximal histidine, respectively. Images of the QM/MM optimized geometries of the protein active sites are shown in the Supplementary Material (Figures S1–S4). For easier comparison, we transformed the local mode force constants $k^a(FeN)$ into relative bond strength orders (BSO) according to the generalized Badger rule derived by Cremer, Kraka, and coworkers[94,95] via a power relationship in the form of $BSO = A(k^a)^B$. Two reference molecules with known BSO and force constants are utilized to obtain the parameters for A and B, with the constraint that a zero value for the force constant $k^a(AB)$ yields a zero BSO value. For the metal-ligand bonds such as FeN bonds we utilized Mayer bond orders[96–98] instead of defining BSO = 1 for single and BSO = 2 for double bonds. In past studies involving transition metal bonding, Mayer bond orders have turned out to be a better choice.[61,62,78,99] Using Mayer bond orders for the single bond in FeH (BSO = 0.8711, k^a = 1.967 mDyn/Å) and the double bond in FeN (BSO = 1.9288, k^a = 3.393 mDyn/Å) evaluated at the PBE0/6-31G(d,p) level of theory, we obtained values of 0.3247 and 1.4584 for parameters A and B, respectively.

We complemented LMA with features of the analysis of the electron density $\rho(\mathbf{r})$ via Bader's QTAIM theory.[100–102] The covalent character of the FeN bonds, in particular, was determined via the Cremer–Kraka criterion,[103,104] which is based on the local electron density $H(\mathbf{r}) = G(\mathbf{r}) + V(\mathbf{r})$, where the kinetic energy density is $G(\mathbf{r})$ (positive, destabilizing) and the potential energy density is $V(\mathbf{r})$ (negative, stabilizing). For bond critical point $\mathbf{r}_b$ of $\rho(\mathbf{r})$ between two bonded atoms AB, if $H(\mathbf{r}_b)$ is negative, the character of the AB bond is predominantly covalent, whereas a positive $H(\mathbf{r}_b)$ value indicates a predominantly electrostatic character. In addition we analyzed the atomic NBO charges of the Fe and N atoms involved in FeN bonding.[105,106]

All Cb5 geometry optimizations and normal vibrational mode analyses were based on the hybrid QM/MM methodology,[107,108] where starting coordinates were taken from the X-ray structures of these proteins (see Table 1) using the following procedure. For X-ray structures with two or more two polypeptide chains, only chain A was used. Missing hydrogen atoms of the experimental structure were added using AMBER,[109] and the molecular complex was neutralized by counter-ions. The heme group of the protein was surrounded by a sphere of TIP3P water molecules[110] extending to 16 Å, and the initial minimization of the protein was performed at the molecular mechanical (MM) level of theory using AMBER. The minimized structure was then divided into a QM part which included the heme group and both the distal and proximal histidine side chains (Figure 1a, average number of QM atoms: 100), whereas the MM part included the remaining atoms (average number of MM atoms: 2020). Chemical bonds between QM and MM parts were cut and free valences of the QM part were filled with hydrogen atoms. QM/MM geometry optimizations were performed without any constraints at the PBE0/6-31G(d,p)/AMBER level of theory[111,112] with the ONIOM method applying scaled electronic embedding.[113] All subsequent frequency calculations terminated without imaginary frequencies, identifying all optimized protein complexes as local minima. In order to analyze the effects of the protein environment, we calculated for comparison gas phase models **GAS** of the bishistidyl hemoproteins active site (see Figure 1b) at the PBE0/6-31G(d,p) level of theory. The PBE0 functional was used in our investigations because of its good performance for transition metals complexes[111,114–116] supported by the fact that the calculated FeN bond length of 1.965 Å of the ferric state gas phase model almost matched the corresponding X-ray value of 1.970 Å in [Fe(III)(meso-tetraphenylporphyrin)$^{2-}$ (1-methyl-imidazole)$_2$]ClO$_4$.[117]

QM/MM and gas phase calculations for the ferric (Fe$_{III}$) and the ferrous (Fe$_{II}$) oxidation states were performed with Gaussian.[118] The QM/MM Hessians from the protein the QM Hessians from the gas phase calculations were used as input for subsequent LMA analyses utilizing our LModeA program.[119] The QTAIM analysis was performed with the AIMALL program[120] and NBO charges were calculated utilizing the NBO analysis implemented in Gaussian16.

Results and Discussion

This section starts with an individual discussion of distal and proximal FeN bond properties for the ferric and ferrous states (Figure 3 and Figure 4). Tables S1–S4 of the Supporting Material summarize the corresponding bond properties including bond length R, local mode force stretching constant k^a(FeN) and corresponding bond strength order BSO, local mode frequency ω^a, energy density at a bond critical point H$_\rho$ and the Fe and N atomic charge difference ΔQ. This is followed by the analysis of overall trends of the FeN distal and axial bond properties in ferric and ferrous states (Figure 5). In the final part of this section, the axial NFeN bond angles for ferric and ferrous states (Figure 6) are analyzed. The corresponding data, collecting axial NFeN bond angles α, local mode force constants k^a(NFeN) and corresponding local mode bending frequencies ω^a for the ferric and ferrous states can be found in Table S5 of the Supporting Material. Images or the active sites of the twelve Cb5s are
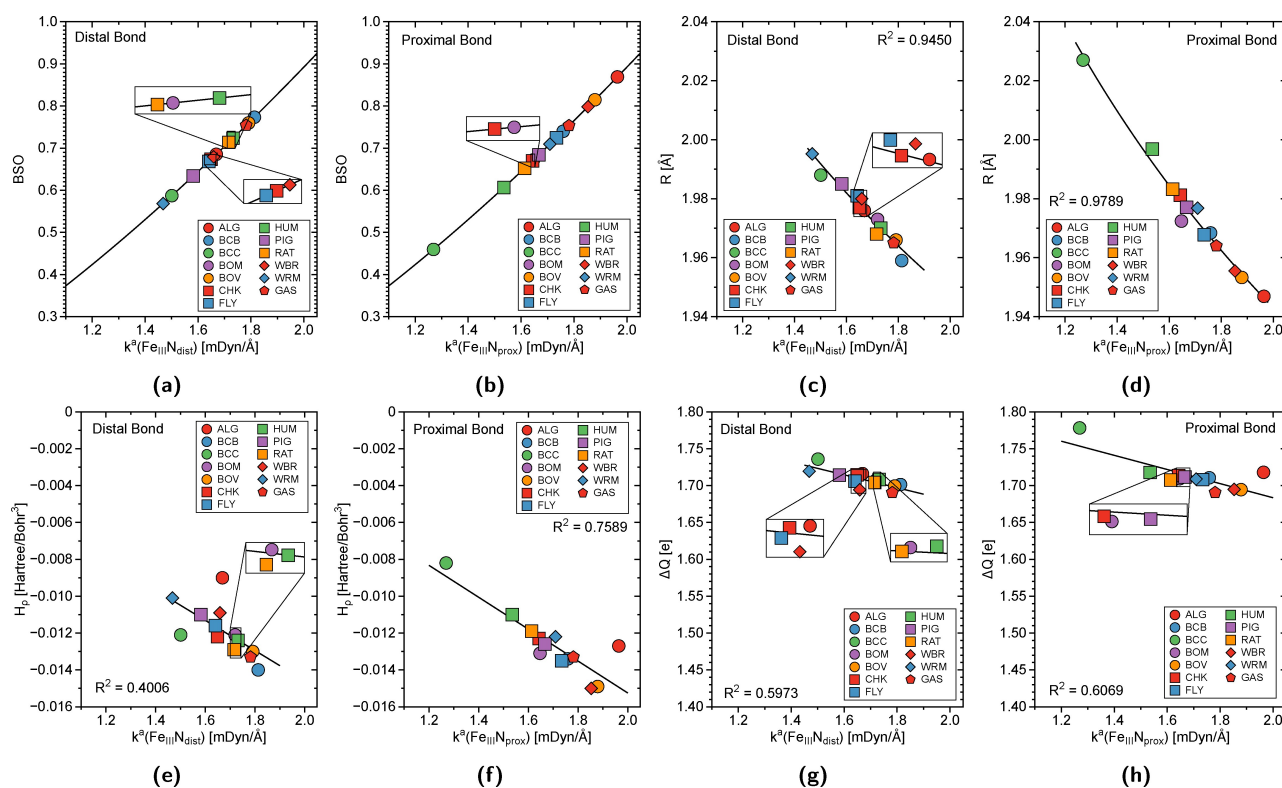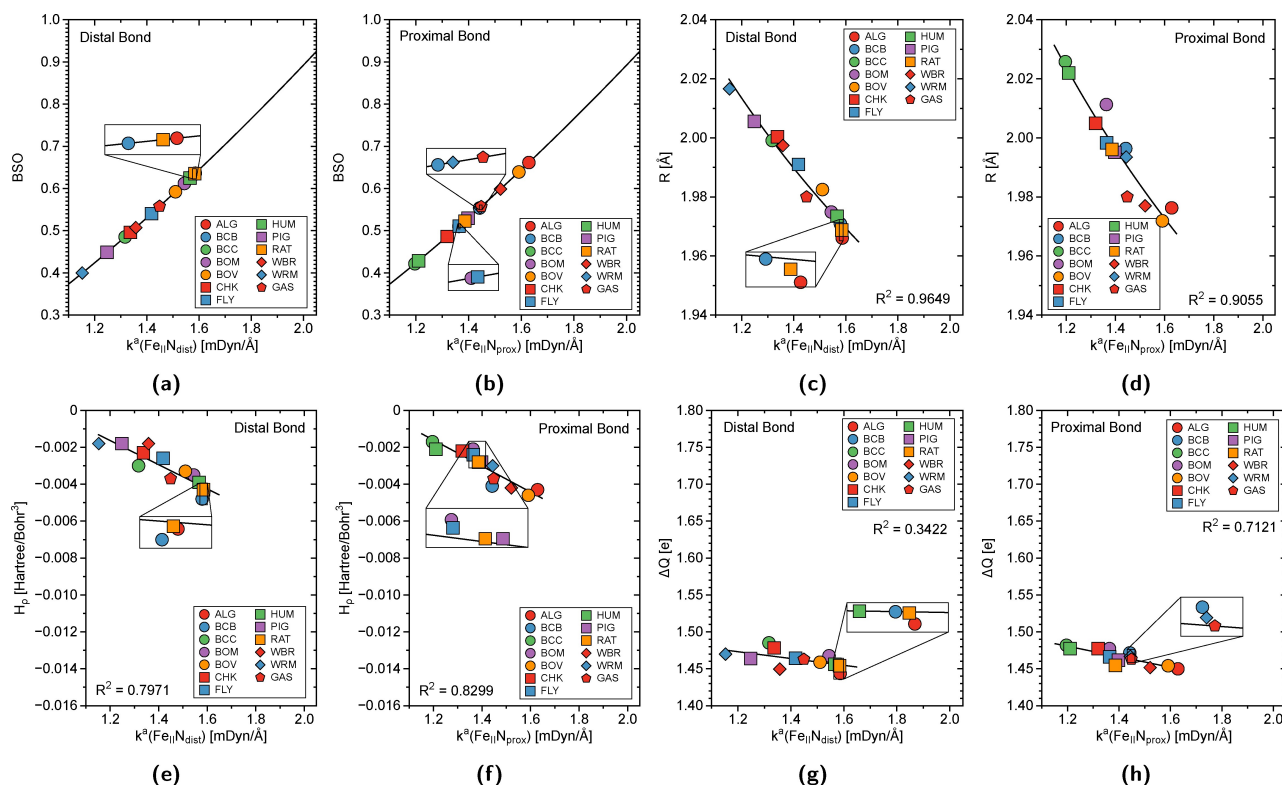

Figure 3. FeN bond properties in the ferric state. **(a)** Bond strength order BSO as a function of local mode force constant k^a(Fe$_{III}$N$_{dist}$); **(b)** BSO as a function of k^a(Fe$_{III}$N$_{prox}$); **(c)** correlation between bond length R and k^a(Fe$_{III}$N$_{dist}$); **(d)** Correlation between R and local mode force constant k^a(Fe$_{III}$N$_{prox}$); **(e)** Correlation between energy density H$_{rho}$ and k^a(Fe$_{III}$N$_{dist}$); **(f)** Correlation between H$_\rho$ and k^a(Fe$_{III}$N$_{prox}$); **(g)** Correlation between charge difference ΔQ and k^a(Fe$_{III}$N$_{dist}$); **(h)** Correlation between ΔQ and k^a(Fe$_{III}$N$_{prox}$). For protein labels see Table 1.

ChemPhysChem

Research Article
doi.org/10.1002/cphc.202401098

**Chemistry
Europe**
European Chemical
Societies Publishing

Figure 4. FeN bond properties in the ferrous state. **(a)** Bond strength order BSO as a function of local mode force constant $k^a(Fe_{III}N_{dist})$; **(b)** BSO as a function of $k^a(Fe_{III}N_{prox})$; **(c)** Correlation between bond length R and $k^a(Fe_{III}N_{dist})$; **(d)** Correlation between R and local mode force constant $k^a(Fe_{III}N_{prox})$; **(e)** Correlation between energy density H_{rho} and $k^a(Fe_{III}N_{dist})$; **(f)** Correlation between H_ρ and $k^a(Fe_{III}N_{prox})$; **(g)** Correlation between charge difference ΔQ and $k^a(Fe_{III}N_{dist})$; **(h)** Correlation between ΔQ and $k^a(Fe_{III}N_{prox})$. For protein labels see Table 1.

shown in Figures S1–S4 as well as additional correlations between local stretching and bending force constants are depicted in Figure S5 of the Supporting Material. This is followed by optimized QM/MM coordinates of all heme groups.

FeN Distal Bonds in the Ferric State

According to Figure 3a and Table S1, the weakest $Fe_{III}N_{dist}$ bond ($k^a = 1.468$ mDyn/Å) is observed for **WRM** from the large round-worm of pig, which adapts a unique structure with an additional α-helix and a disulfide bridge linking the head to the tail part of the protein. This sets **WRM** apart from the other eleven Cb5s investigated in this work. On the other side of the spectrum, **BCB** exhibits the strongest $Fe_{III}N_{dist}$ bond ($k^a = 1.813$ mDyn/Å) in this series. The average $k^a(Fe_{III}N_{dist})$ value for the twelve Cb5s of our study is 1.662 mDyn/Å, which is lower than the corresponding gas phase value of $k^a = 1.782$ mDyn/Å, reflecting the influence of protein effects on the FeN bond strength. According to Figure 3c the $Fe_{III}N_{dist}$ bond strengths correlate with the corresponding bond lengths ($R^2 = 0.9450$), following the rule that stronger bonds are generally shorter bonds, which is not always the case, as documented in the literature.[121–123] Figure 3e illustrates the relationship between the local mode force constant $k^a(Fe_{III}N_{dist})$ and the energy density H_ρ. Although no significant correlation is observed ($R^2 = 0.4006$), stronger $Fe_{III}N_{dist}$ bonds tend to be more covalent, as

reflected by more negative H_ρ values. Along the same lines, as illustrated in Figure 3g, there is some trend between $k^a(Fe_{III}N_{dist})$ and the charge difference $\Delta Q(FeN)$ between the Fe and N atom involved in this bond ($R^2 = 0.5973$) indicating that stronger $Fe_{III}N_{dist}$ bonds are less polar.

FeN Proximal Bonds in the Ferric State

As reflected by Figure 3b and Table S2 the weakest $Fe_{III}N_{prox}$ bond is observed for **BCC** ($k^a = 1.269$ mDyn/Å), which has also the second weakest **BCC** distal bond (($k^a = 1.501$ mDyn/Å). The strongest $Fe_{III}N_{prox}$ bond is found for **ALG** from the Green Alga Virus ($k^a = 1.964$ mDyn/Å), which is the strongest FeN bond among all Cb5s investigated in this study. The average strength of the $Fe_{III}N_{prox}$ bonds ($k^a = 1.728$ mDyn/Å, excluding the **BCC** value) is close to the gas phase value of 1.781 mDyn/Å. It is interesting to note that the proximal **BCC** k^a value of 1.269 mDyn/Å is significantly smaller than the average value of 1.728 mDyn/Å, suggesting a specific orientation of the heme group of **BCC**, i.e., a strongly rotated heme group compared to those of the other Cb5s of this study, as indicted in Figures S1–S4 (Supplementary Material). According to Figure 3d, the $Fe_{III}N_{prox}$ bond strength correlates ($R^2 = 0.9789$) with the bond length. As reflected in Figure 3f and Figure 3h, respectively, there is no signifiant correlation between bond strength and covalency ($R^2 = 0.7589$) and between bond strength and the
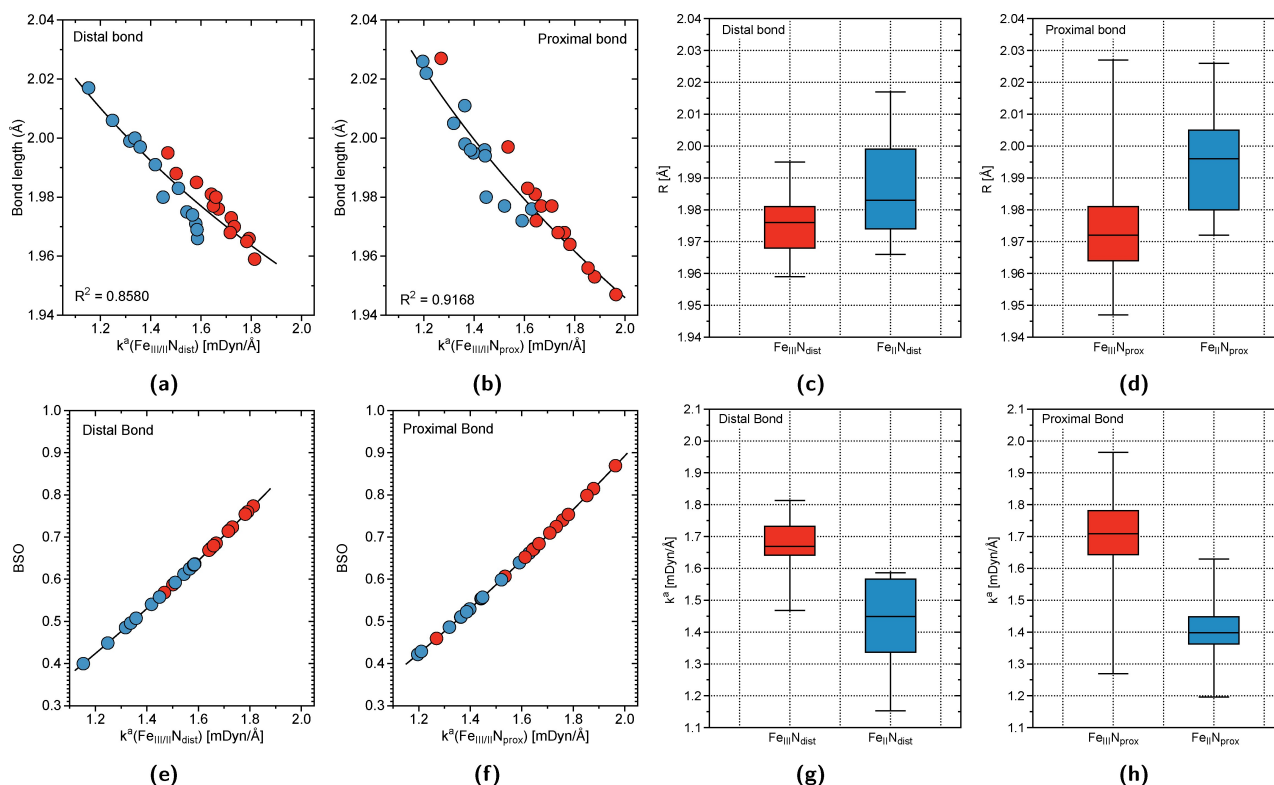
ChemPhysChem

Research Article
doi.org/10.1002/cphc.202401098

Chemistry Europe
European Chemical
Societies Publishing

Figure 5. Comparison of axial FeN bonds in the ferric and ferrous states. **(a)** Bond length as a function of local mode force constant $k^a(Fe_{III/II}N_{dist})$; ferric state (red color) and ferrous state (blue color); **(b)** Bond length as a function of $k^a(Fe_{III/II}N_{prox})$; ferric state (red color) and ferrous state (blue color); **(c)** Box-and-whisker plot of the distal bond lengths; ferric state (red color) and ferrous state (blue color); **(d)** Box-and-whisker plot of the proximal bond lengths; ferric state (red color) and ferrous state (blue color). textbf(e) Bond order BSO as a function of local mode force constant $k^a(Fe_{III/II}N_{dist})$; ferric state (red color) and ferrous state (blue color); **(f)** BSO as a function of $k^a(Fe_{III/II}N_{prox})$; ferric state (red color) and ferrous state (blue color); **(g)** Box-and-whisker plot of $k^a(Fe_{III/II}N_{dist})$; ferric state (red color) and ferrous state (blue color); **(h)** Box-and-whisker plot of $k^a(Fe_{III/II}N_{prox})$; ferric state (red color) and ferrous state (blue color).

charge difference $\Delta Q(FeN)$ ($R^2 = 0.6069$). Overall, we observe the same general trend reflected in the properties of the $Fe_{III}N_{prox}$ bonds as in their distal counterparts, namely that a stronger FeN bond is also shorter, more covalent, and less polar.

FeN Distal Bonds in the Ferrous State

According to Table S3 and Figure 4a the weakest $Fe_{II}N_{dist}$ bond ($k^a = 1.153$ mDyn/Å) is found for **WRM**, which is also the weakest axial FeN bond among all Cb5 structures investigated in this study. The strongest $Fe_{II}N_{dist}$ bond ($k^a = 1.586$ mDyn/Å) is that of **ALG**. The average strength of the $Fe_{II}N_{dist}$ bonds is with a k^a values of 1.433 mDyn/Å, similar to the strength of this bond of the gas phase model ($k^a = 1.449$ mDyn/Å). According to Figures 4c, 4e and 4g, $k^a(Fe_{II}N_{dist})$ correlates with bond length R ($R^2 = 0.9649$) and to a lesser extent with the bond covalency ($R^2 = 0.7971$). There is no correlation between bond strength and the charge difference $\Delta Q(FeN)$ ($R^2 = 0.3422$). Overall, the properties of the $Fe_{II}N_{dist}$ bond show the same trend as observed for the $Fe_{III}N_{dist}$ and $Fe_{III}N_{prox}$ bonds, i.e., stronger bonds are shorter and tend to be more covalent.

FeN Proximal Bonds in the Ferrous State

According to Table S4 and Figure 4b, **BCC** has the weakest $Fe_{III}N_{prox}$ bond in this series with a k^a value of 1.196 mDyn/Å, whereas the strongest FeN bond is found for **ALG** ($k^a = 1.629$ mDyn/Å). The average strength of this bond comes with a k^a value of 1.405 mDyn/Å close to the strength of the corresponding gas phase FeN bond ($k^a = 1.448$ mDyn/Å). $k^a(Fe_{II}N_{prox})$ correlates with bond length R ($R^a = 0.9055$, Figure 4d), and to some extent with H_ρ ($R^a = 0.8299$, Figure 4f), and the charge difference $\Delta Q(FeN)$ ($R^a = 0.7121$, Figure 4h).

Overall Comparison of FeN Distal and Axial Bonds in Ferric and Ferrous States

Figure 5a and 5b illustrate the overall correlation between FeN bond length R and local mode force constant k^a for the distal and proximal bonds in both the ferric (red color) and the ferrous (blue color) states, respectively, and Figure 5c and 5d the corresponding statistics of the bond properties in the form of the box-and-whisker plots. As discussed above, bond length changes among the twelve Cb5s are only marginal for both distal and proximal FeN bonds, with a slightly larger bond length range for the proximal bonds. Compared to hexacoordi-
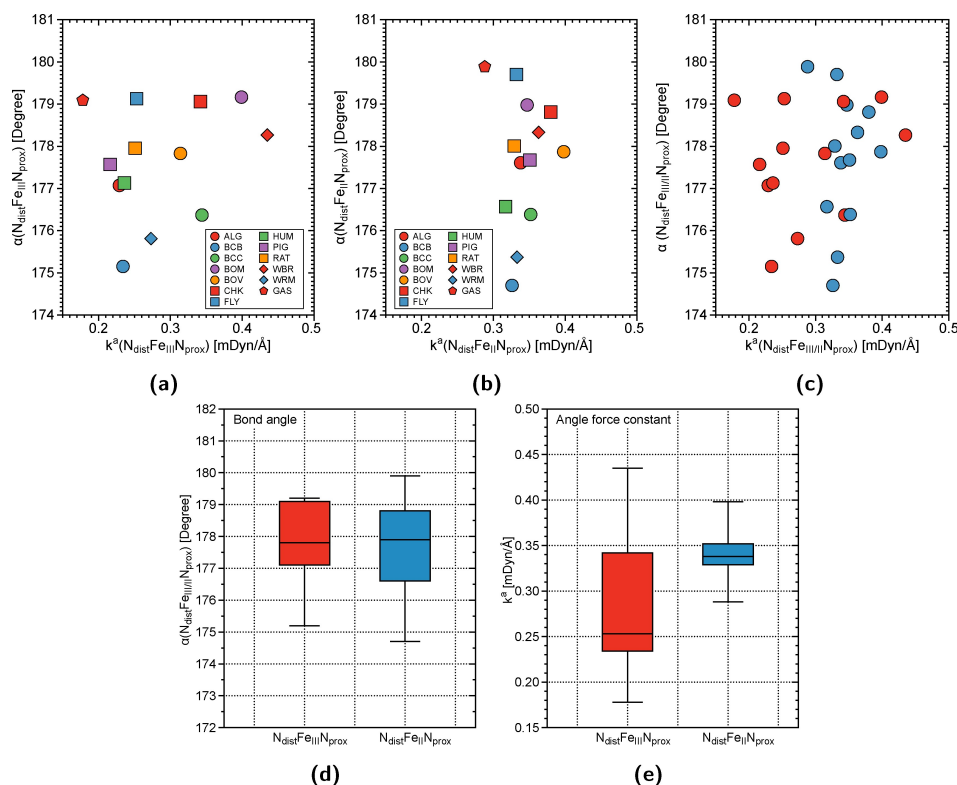
ChemPhysChem

Research Article
doi.org/10.1002/cphc.202401098

Chemistry Europe
European Chemical
Societies Publishing

Figure 6. Axial NFeN bond angle correlations in the ferric and ferrous states. **(a)** Correlation between force constant $k^a(NFe(III)N)$ and NFe(III)N bond angle $\alpha(NFe(III)N)$; **(b)** Correlation between force constant $k^a(NFe(II)N)$ and bond angle $\alpha NFe(II)N$; **(c)** Force constant $k^a(NFeN)$ versus NFeN bond angle for both the ferric state (red color) and ferrous state (blue color), **(d)** Box-and-whisker plot of axial NFeN bond angles; **(e)** Box-and-whisker plot of the corresponding bending force constants; ferric state (red color) and ferrous state (blue color).

nate myoglobin-CO complexes (average R = 1.75 Å, BSO range: 1.2–1.5)[78] and neuroglobin-CO complexes (average R = 1.77 Å, BSO range: 0.85–1.0)[79] both with a single FeN linkage via the proximal histidine, the proximal cytochrome b5 linkage exhibits considerably larger R values, reflecting that the logistics of a bishistidyl linkage is more complex and prevents a more tighter FeN approach. Figure 5a reveals a concentration of the ferric bond lengths on the smaller side for the distal FeN bond, whereas, as obvious from Figure 5b ferric bond length values for the proximal FeN bond also stretch in to the larger bond length side.

According to Figure 5c, the median of the distal FeN bond lengths in the ferric state (red color) has a value of 1.976 Å, which is close the median in the ferrous state (blue color) with a value of 1.983 Å. However, the range of the distal FeN bond length values n the ferric state is smaller than that of the ferrous state (0.036 and 0.051 Å, respectively). Similarly, the interquartile range (IQR, displaying a difference between the 75th and 25th percentiles of the data) of this bond in the ferric state) is smaller than that of the ferrous state (0.013 and 0.025 Å, respectively), which indicates on a larger concentration of the bond length values around its median for the distal bond length in the ferric state. For the proximal FeN bond (see Figure 5d), the median of the bond length in the ferric state is smaller than that in the ferrous state (1.972 and 1.996 Å, respectively), reflecting that the change from the ferric to ferrous state makes the FeN proximal bond overall longer. In

contrast, the bond length range in the ferric state is much greater than in the ferrous state (0.080 and 0.054 Å, respectively), which is opposite to the IQR values of this bond (0.017 and 0.025 Å, respectively), indicating on a larger concentration of the bond length around its median value, similar as for the distal bond.

Based on the LMA results depicted in Figure 5e–5 h we can draw the conclusion that overall the ferric Fe(III)N Cb5s bonds are stronger than their ferrous Fe(II)N counterparts for both distal and proximal bonds for all Cb5s investigated in this work, independent of their origin. The change of the Fe oxidation state from ferric to ferrous makes both the distal and the proximal FeN bonds weaker as illustrated in Figures 5e and 5f. This is also reflected by the corresponding average k^a values of 1.662 mDyn/Å (Fe$_{III}$N$_{dist}$ bonds), 1.689 mDyn/Å (Fe$_{III}$N$_{prox}$ bonds), 1.433 mDyn/Å (Fe$_{II}$N$_{dist}$ bonds), and 1.405 mDyn/Å (Fe$_{II}$N$_{prox}$ bonds, respectively. In comparison, the corresponding gas phase values are 1.782 mDyn/Å for the Fe$_{III}$N$_{dist}$ bond, 1.781 mDyn/Å for the Fe$_{III}$N$_{prox}$ bond, 1.449 mDyn/Å for the Fe$_{II}$N$_{dist}$ bond, and 1.448 mDyn/Å for the Fe$_{II}$N$_{prox}$ bond.

The box-and-whisker graphs of k^a for the distal FeN and proximal FeN bonds in both oxidation states (Figure 5g and Figure 5h) provide further details about the distribution of the bond strength data. k^a(Fe$_{III}$N$_{dist}$) values range from 1.468 to 1.813 mDyn/Å, covering a range of 0.35 mDyn/Å. k^a(Fe$_{III}$N$_{prox}$) values range from 1.269 to 1.964 mDyn/Å covering a significantly larger range of 0.80 mDyn/Å primarily caused by the

ChemPhysChem

Research Article
doi.org/10.1002/cphc.202401098

Chemistry
Europe
European Chemical
Societies Publishing

small k^a of 1.269 mDyn/Å for **BCC**, which as discussed above results from the unique placement of the heme co-factor in the protein. In comparison, $k^a(Fe_{II}N_{dist})$ values range from 1.153 to 1.586 mDyn/Å covering a range of 0.43 mDyn/Å. $k^a(Fe_{II}N_{prox})$ values range from 1.196 to 1.629 mDyn/Å covering the same range of 0.43 mDyn/Å. The median values of 1.669 mDyn/Å and 1.449 mDyn/Å of the distal FeN bonds for ferric and ferrous states, respectively as well as the median values of 1.709 mDyn/Å and 1.398 mDyn/Å of the distal FeN bonds for ferric and ferrous states, respectively clearly identifies the FeN bonds of the ferric state as the stronger ones. The distal ferric FeN bonds have a smaller IQR value of 0.091 mDyn/Å, i.e., a tighter concentration of values than the distal ferrous FeN bonds with an IQR value of 0.229 mDyn/Å. It is interesting to note that for the proximal FeN bonds the opposite holds, where the ferrous FeN bonds show a somewhat larger spread with an IQR value of 0.138 mDyn/Å compared to the ferrous IQR value of 0.085 mDyn/Å. As revealed by Figure 5e and 5f, distal bonds (ferric and ferrous) cover a BSO range from 0.400 (see also Table S3) to 0.773 (see also Table S1) and proximal bonds (ferric and ferrous) from 0.442 (see also Table S4) to 0.869 (see also Table S2), which comes close to a single bond.

LMA properties are sensitive to subtle differences in the protein geometry, as reflected by the pronounced variations in local stretching force constant values across various Cb5 structures. According to our LMA results, in the ferric state, the weakest FeN bond observed in our calculations is that of **BCC** at the proximal side ($k^a = 1.269$ mDyn/Å) due to the rotated orientation of the protein's heme group,[3] which is unusual for classical Cb5 proteins. The rotation of the heme group inside the heme pocket changes the non-bonded interactions with the side chains of the amino acids in the heme pocket, which can lower the strength of chemical bonds between Fe and both axial histidines. **BCC**'s distal FeN bond is also relatively weak ($k^a = 1.501$ mDyn/Å). In contrast, the strongest FeN bond in the ferric state is found for **ALG** at the proximal side ($k^a = 1.964$ mDyn/Å); the distal FeN bond is relatively strong as well ($k^a = 1.669$ mDyn/Å). **ALG** is a viral version of Cb5, and in contrast to all other microsomal cytochrome Cb5s, it lacks a hydrophobic C-terminal anchor.[1] In the ferrous state, the weakest FeN bond is observed for **WRM** at the distal side ($k^a = 1.153$ mDyn/Å), whereas its proximal FeN bond is relatively stronger ($k^a = 1.444$ mDyn/Å). **WRM**, a Cb5 isolated from the large roundworm of pig, has an additional α-helix and positively charged residues on the surface domain which are capable of interacting with redox partners. Unique to **WRM**, the additional α-helix rotates the heme group; this rotation of the heme group is essential for interactions with other reaction partners[16] and also appears to be responsible for a relatively weak FeN bond at the proximal side – similar to what was observed in our calculations of the **BCC** protein. The strongest FeN bond in the ferrous state is observed for **ALG** at the proximal side ($k^a = 1.629$ mDyn/Å); **ALG**'s distal FeN bond is also relatively strong ($k^a = 1.586$ mDyn/Å). It is interesting to note that those two axial FeN bonds are also relatively strong in the ferric state as well, as discussed above. Although the differences between the FeN bond lengths of the **BCC**, **ALG**, and **WRM** are on the order of

10^{-2} Å, these small variations between the Cb5 structures' geometries are highlighted by the corresponding yet more pronounced variations in the local mode force constants, which are on the order of 10^{-1} mDyn/Å.

The differences in axial FeN bond strengths between the two oxidation states of the investigated Cb5s are also reflected in other bond properties. According to Figure 3c and 3d as well as Figure 4c and 4d, the average $Fe_{III}N_{dist}$ bond length is smaller than the average $Fe_{II}N_{dist}$ bond length (R = 1.977 and 1.987 Å, respectively), and the average $Fe_{III}N_{prox}$ bond length is smaller than the average $Fe_{II}N_{prox}$ bond length (R = 1.972 and 1.987 Å, respectively). Similarly, according to Figure 3e and 3f as well as Figure 4e and 4f, the $Fe_{III}N_{dist}$ bond is more covalent than the $Fe_{II}N_{dist}$ bond (average $H_\rho = -0.0118$ and -0.0031 Hartree/Bohr^3, respectively); along the same lines the $Fe_{III}N_{prox}$ bond is more covalent than the $Fe_{II}N_{prox}$ bond (average $H_\rho = -0.0128$ and -0.0030 Hartree/Bohr^3, respectively). In other words, Fe(III)N bonds are generally more covalent than their Fe(II)N counterparts.

Overall, these results confirm recent results for a series of other bishistidyl hemoproteins from bacteria, animals, human, and plants, which involved two cytoglobins, ten hemoglobins, two myoglobins, six neuroglobins, and six phytoglobins[84] where we also found that the axial FeN bond length varies only marginal, with a slightly broader range covered by the proximal FeN bonds, and that the change of the protein oxidation state from ferric to ferrous state generally makes the FeN bond weaker, whether proximal or distal.

Axial NFeN Bond Angle in Ferric and Ferrous States

In addition to local bond stretching force constants LMA provides also local bond angle force constants reflecting the bond angle stiffness (larger values) or flexibility (smaller values).[84,124,125] In this study we utilized the local angle force constants $k^a(NFeN)$ for both oxidation states as a tool to assess the axial angle stiffness/flexibility in the Cb5 active site and to monitor changes in the axial heme framework caused by different protein environments. Table S5 collects axial NFeN bond angle α, local mode force constant $k^a(NFeN)$ and corresponding local mode bending frequency ω^a data for both the ferric and ferrous states. Figure 6a shows the correlation between force constant $k^a(NFe(III)N)$ and NFe(III)N bond angle and Figure 6b shows the correlation between force constant $k^a(NFe(II)N)$ and NFe(II)N bond angle. Figure 6c summarizes the correlation between force constant $k^a(NFeN)$ and NFeN bond angle for both the ferric state (red color) and ferrous state (blue color) in a more compact form. There are no correlations between these two properties. As revealed by Figure S5 of the Supporting Material, for both the ferric and ferrous oxidation states, we do not observe any significant correlation between local mode stretching force constants $k^a(NFe)$ and bending force constants $k^a(NFeN)$; we also do not observe any correlations between the $k^a(NFe(III)N)$ and $k^a(NFe(II)N)$ bending force constants.

ChemPhysChem

Research Article
doi.org/10.1002/cphc.202401098

Chemistry
Europe
European Chemical
Societies Publishing

According to Figure 6c and the data in Table S5, there is only a marginal deviation of the axial NFeN bond angle from linearity for all members of both the ferric state (bond angle range: 179.2° **BOM**–175.2° **BCB**) and the ferrous state (bond angle range: 179.7° **FLY**–174.78° **BCB**). In comparison the gas phase NFeN bond angles are 179.1° and 179.9° for the ferric and ferrous states, respectively. Bis-histidyl coordination of the heme co-factor does not lead to significant NFeN bending, i.e, no significant structural changes compared to the gas phase model for both ferric and ferrous state. On the other hand, there are noticeable differences in the angle stiffness as reflected by the bending force constants k^a(NFeN). As previously mentioned, the local mode bending force constant k^a is a second order property in contrast to the bond angle, which is a first order property. As such, local mode force constants k^a are generally more sensitive to electronic environment than geometric descriptors; as shown by our data, this sensitivity is seen especially for bond angle stiffness/flexibility. Figure 6c shows that the range of the ferric local mode force constants k^a(NFe(III)N) is twice as large as that of the ferrous local mode force constants k^a(NFe(II)N) (0.257 versus 0.110 mDyn/Å, respectively, with the ferrous bond angles leaning more towards larger k^a(NFeN) values, i.e., stiffer bond angles). On the average the axial NFeN bond angle in the protein is stiffer than that in the gas phase (average $k^a = 0.294$ versus 0.178 mDyn/Å, respectively, for the ferric state; average $k^a = 0.347$ versus 0.288 mDyn/Å, respectively for the ferrous state), which indicates that the protein environment of Cb5 generally makes that bond angle less flexible, because in the protein both histidine side chains are chemically bonded to and confined by the protein backbone.

Figure 6d and 6e show the box-and-whisker plots of bond angles and bending force constants, respectively, for the ferric and ferrous oxidation states. The median values of the axial NFe(III)N and NFe(II)N bond angles are 177.8 and 177.9, respectively, indicating that the heme-coordinated histidine ligands slightly deviate from a perfectly linear orientation within the protein, as previously mentioned. The distribution of angles across Cb5 species is also relatively tight, with small IQR values of 2° for the ferric state and 2.2° for the ferrous state. In contrast, there are pronounced differences between the bending force constants of the ferric and ferrous states. The median bending force constants of the ferric and ferrous states are 0.25 mDyn/Å and 0.34 mDyn/Å, respectively; thus, the bond angles become stiffer and less flexible upon reduction of the heme iron. In addition, as reflected by the IQR values, we find a significant tighter concentration of k^a(NFe(II)N) values compared to the k^a(NFe(III)N) values, a difference which points to a decrease in the variation of bond angle stiffness/flexibility upon reduction.

Conclusions and Outlook

Using LMA combined with the QM/MM methodology, we analyzed in this study the iron-histidine coordination in a series of twelve Cb5s isolated from different species with a focus on

the strength of the FeN distal/proximal bonds and the stiffness of the axial NFeN bond angle. The investigation was augmented by the topological analysis of the electron density and NBO analysis for each Cb5 structure. This led to the following major findings:

- *FeN bonds:* Bond length variations across species are relatively small, although proximal bonds cover a slightly larger range of bond lengths than distal bonds. For both distal and proximal bonds, we observe that ferric bonds tend to be slightly shorter than ferrous bonds. This difference in bond lengths, albeit small, is correlated with a pronounced difference in local stretching force constants. Examining the influence of the protein environment on bond strength, we observed that the protein environment of the investigated Cb5s, across all species, alters the strength of both the FeN distal and proximal bonds in both oxidation states – relative to the strength of their counterparts in the gas phase models. Overall, we found that the distal and proximal FeN bonds become weaker, longer, and less covalent upon reduction of the heme iron for all Cb5s investigated in this work.

- *NFeN bond angles:* The axial NFeN bond angles deviate only slightly from a perfectly linear orientation of the two heme-coordinated histidine ligands. While we found a correlation between FeN bond length and bond strength for both heme iron oxidation states, we did not find a correlation between NFeN bond angle and angle stiffness. In addition, the stiffness of the NFeN bond angle does not correlate with the strength of the individual FeN bonds. Overall, the reduction of the heme iron stiffens the NFeN bond angle, and the protein environment, due to space confinement, also stiffens the NFeN bond angle (compared to the gas phase models). These changes effectively reduce the flexibility of the histidine ligands within the investigated Cb5 structures.

- *Cb5 species of origin:* LMA is a sensitive probe for detecting differences between the FeN bond strengths of Cb5 structures from varying species of origin, reflecting differences in the protein structure, as demonstrated through the comparison of FeN stretching force constants for the **WRM**, **BCC** and **ALG** structures.

The LMA bond strength and bond angle stiffness, as second order properties, were sensitive to the redox-induced changes to both the electronic and geometric structure of the heme group and may therefore serve as useful feature data for the training and refinement of future ML models designed to predict the redox potentials of Cb5 and Cb5-like proteins. If successful, this approach would demonstrate how LMA data could complement the aforementioned feature data (i.e., geometric structure, electronic/bonding properties, and descriptors of the surrounding protein environment) currently used in the development of such models. Furthermore, such work could be even further extended by incorporating relevant LMA data for other metalloproteins as well during model training, thereby potentially paving the way for generalized and better-trained ML models which could inform the design of synthetically enhanced metalloproteins whose redox potentials are fine-tuned for various bioelectrocatalytic applications. In future studies, it would also be of interest to evaluate the changes in

ChemPhysChem

Research Article
doi.org/10.1002/cphc.202401098

Chemistry
Europe
European Chemical
Societies Publishing

the redox potential of the Cb5 protein due to synthetic modifications of the FeN bond strength and NFeN bond angle stiffness. To the best of our knowledge, the influence of modifications to these two descriptors on the redox potential of the Cb5 protein has not been previously examined in the literature. A combined experimental and computational analysis of this question would provide critical insights into how the modification of the protein's primary coordination sphere may alter its redox potential and, by extension, its ET properties.

Acknowledgements

Conflict of Interests

Please enter any conflict of interest to declare.

Data Availability Statement

The data that support the findings of this study are available in the supplementary material of this article.

[1] E. L. Reid, K. D. Weynberg, J. Love, M. N. Isupov, J. A. Littlechild, W. H. Wilson, S. L. Kelly, D. C. Lamb, M. J. Allen, *FEBS Lett.* **2013**, *587*, 3633.

[2] V. Kostanjevečki, D. Leys, G. Van Driessche, T. E. Meyer, M. A. Cusanovich, U. Fischer, Y. Guisez, J. Van Beeumen, *J. Biol. Chem.* **1999**, *274*, 35614.

[3] S. Teakel, M. Marama, D. Aragão, S. Tsimbalyuk, E. R. R. Mackie, T. P. Soares da Costa, J. K. Forwood, M. A. Cahill, *FEBS Lett.* **2022**, *596*, 2409.

[4] P. Yao, J. Wu, Y.-H. Wang, B.-Y. Sun, Z.-X. Xia, Z.-X. Huang, *Europ. J. Biochem.* **2002**, *269*, 4287.

[5] P. Yao, Y.-H. Wang, Y. Xie, Z.-X. Huang, *J. Electroanal. Chem.* **1998**, *445*, 197.

[6] R. C. E. Durley, F. S. Mathews, *Acta Crystallogr. Sect. D* **1996**, *52*, 65.

[7] C. Kisker, H. Schindelin, A. Pacheco, W. A. Wehbi, R. M. Garrett, K. V. Rajagopalan, J. H. Enemark, D. C. Rees, *Cell* **1997**, *91*, 973.

[8] L. Wang, A. B. Cowley, S. Terzyan, X. Zhang, D. R. Benson, *Proteins Struct. Funct. Bioinf.* **2007**, *67*, 293.

[9] V. M. Guzov, H. L. Houston, M. B. Murataliev, F. A. Walker, R. Feyereisen, *J. Biol. Chem.* **1996**, *271*, 26637.

[10] S. Parthasarathy, A. Altuve, S. Terzyan, X. Zhang, K. Kuczera, M. Rivera, D. R. Benson, *Biochemistry* **2011**, *50*, 5544.

[11] T. Aono, Y. Sakamoto, M. Miura, F. Takeuchi, H. Hori, M. Tsubaki, *J. Biomed. Sci.* **2010**, *17*, 1.

[12] Y. Hirano, S. Kimura, T. Tamada, *Acta Crystallogr. Sect. D* **2015**, *71*, 1572.

[13] A. Altuve, S. Silchenko, K.-H. Lee, K. Kuczera, S. Terzyan, X. Zhang, D. R. Benson, M. Rivera, *Biochemistry* **2001**, *40*, 9469.

[14] M. Rivera, M. A. Wells, F. A. Walker, *Biochemistry* **1994**, *33*, 2161.

[15] Y. Fukuda, J. Kim, T. Inoue, *Prot. Sci.* **2020**, *29*, 1829.

[16] T. Yokota, Y. Nakajima, F. Yamakura, S. Sugio, M. Hashimoto, S. Takamiya, *Biochem. J.* **2006**, *394*, 437.

[17] E. Sjulstok, J. M. H. Olsen, I. A. Solov'yov, *Sci. Rep.* **2015**, *5*, 18446.

[18] J. Liu, S. Chakraborty, P. Hosseinzadeh, Y. Yu, S. Tian, I. Petrik, A. Bhagi, Y. Lu, *Chem. Rev.* **2014**, *114*, 4366.

[19] Y. Lu, N. Yeung, N. Sieracki, N. M. Marshall, *Nature* **2009**, *460*, 855.

[20] P. Hosseinzadeh, Y. Lu, *Biochim. Biophys. Acta Rev. Bioenerg.* **2016**, *1857*, 557.

[21] R. A. Marcus, *Angew. Chem. Int. Ed. Engl.* **1993**, *32*, 1111.

[22] M. Ali, P. Bhardwaj, H. M. Ishqi, M. Shahid, A. Islam, *Molecules* **2023**, *28*, 6209.

[23] L. Era, Y. Kitagawa, N. Yasuda, T. Kamimura, N. Amamizu, H. Sato, K. Cho, M. Okumura, M. Nakano, *Molecules* **2021**, *26*, 6129.

[24] N. Thallaj, *Int. J. Adv. Pharmac. Sci. Res.* **2021**, *4*, 1.

[25] H. Chen, O. Simoska, K. Lim, M. Grattieri, M. Yuan, F. Dong, Y. S. Lee, K. Beaver, S. Weliwatte, E. M. Gaffney, et al., *Chemical Reviews* **2020**, *120*, 12903.

[26] S. Ma, R. Ludwig, *ChemElectroChem* **2019**, *6*, 958.

[27] S. Alferov, V. Coman, T. Gustavsson, A. Reshetilov, C. von Wachenfeldt, C. Hägerhäll, L. Gorton, *Electrochim. Acta* **2009**, *54*, 4979.

[28] R. Takeuchi, A. Suzuki, K. Sakai, Y. Kitazumi, O. Shirai, K. Kano, *Bioelectrochemistry* **2018**, *122*, 158.

[29] Y. Yu, C. Cui, X. Liu, I. D. Petrik, J. Wang, Y. Lu, *J. Am. Chem. Soc.* **2015**, *137*, 11570.

[30] H. Sawai, N. Kawada, K. Yoshizato, H. Nakajima, S. Aono, Y. Shiro, *Biochemistry* **2003**, *42*, 5133.

[31] J. T. Trent, A. N. Hvitved, M. S. Hargrove, *Biochemistry* **2001**, *40*, 6155.

[32] J. T. Trent, S. Kundu, J. A. Hoy, M. S. Hargrove, *J. Mol. Biol.* **2004**, *341*, 1097.

[33] D. de Sanctis, A. Pesce, M. Nardini, M. Bolognesi, A. Bocedi, P. Ascenzi, *IUBMB Life* **2004**, *56*, 643.

[34] A. Pesce, K. Barmpidi, S. Dewilde, C. Estarellas, L. Moens, M. Bolognesi, F. J. Luque, M. Nardini, *J. Inorg. Biochem.* **2023**, *246*, 112289.

[35] J. Uzan, S. Dewilde, T. Burmester, T. Hankeln, L. Moens, D. Hamdane, M. C. Marden, L. Kiger, *Biophys. J.* **2004**, *87*, 1196.

[36] T. R. Weiland, S. Kundu, J. T. Trent, J. A. Hoy, M. S. Hargrove, *J. Am. Chem. Soc.* **2004**, *126*, 11930.

[37] B. J. Smagghe, G. Sarath, E. Ross, J.-l. Hilbert, M. S. Hargrove, *Biochemistry* **2006**, *45*, 561.

[38] B. J. Smagghe, P. Halder, M. S. Hargrove, R. K. Poole, *Chapter Twenty – Measurement of Distal Histidine Coordination Equilibrium and Kinetics in Hexacoordinate Hemoglobins*, vol. 436, pages 359–378, Academic Press **2008**.

[39] G. DeSimone, D. Sbardella, F. Oddone, A. Pesce, M. Coletta, P. Ascenzi, *Cells* **2023**, *10*, 3366.

[40] P. Halder, J. T. Trent III, M. S. Hargrove, *Proteins* **2007**, *66*, 172.

[41] M. Wang, H. Chen, Z. Gu, H. Zhang, W. Chen, Y. Q. Chen, *App. Microbiol. Biotech.* **2013**, *97*, 10255.

[42] A. D. Doroshchuk, L. F. Dmitriev, *Dokl. Biochem. Biophys.* **2013**, *453*, 292.

[43] G. F. Grinstead, J. L. Gaylor, *J. Biol. Chem.* **1982**, *257*, 13937.

[44] E. Hegesh, J. Hegesh, A. Kaftory, *N. Eng. J. Med.* **1986**, *314*, 757.

[45] P. Schröder, D. Obendorf, T. Bechtold, *ChemElectroChem* **2019**, *6*, 3311.

[46] M. Rivera, R. Seetharaman, D. Girdhar, M. Wirtz, X. Zhang, X. Wang, S. White, *Biochemistry* **1998**, *37*, 1485.

[47] M. Wirtz, V. Oganesyan, X. Zhang, J. Studer, M. Rivera, *Faraday Discuss.* **2000**, *116*, 221.

[48] W. Qian, Y.-H. Wang, W.-H. Wang, P. Yao, J.-H. Zhuang, Y. Xie, Z.-X. Huang, *J. Electroanal. Chem.* **2002**, *535*, 85.

[49] S. Sarma, B. Dangi, C. Yan, R. J. DiGate, D. Banville, R. Guiles, *Biochemistry* **1997**, *36*, 5645.

[50] B. Dangi, J. I. Blankman, C. J. Miller, B. F. Volkman, R. Guiles, *J. Phys. Chem. B* **1998**, *102*, 8201.

[51] P. Yao, Y. Xie, Y.-H. Wang, Y.-L. Sun, Z.-X. Huang, G.-T. Xiao, S.-D. Wang, *Protein Eng.* **1997**, *10*, 575.

[52] A. Oliveira, J. Rubio, C. Noble, J. Anderson, J. Anders, A. Mulholland, *J. Chem. Theory Comput.* **2023**, *20*, 385.

[53] J. Cheng, X. Liu, J. VandeVondele, M. Sulpizi, M. Sprik, *Acc. Chem. Res.* **2014**, *47*, 3522.

[54] S. Bhattacharyya, M. T. Stankovich, D. G. Truhlar, J. Gao, *J. Phys. Chem. A* **2007**, *111*, 5729.

[55] S. Jafari, Y. A. T. Santos, M. I. Justin Bergmann, U. Ryde, *Inorg. Chem.* **2022**, *61*, 5991.

[56] B. G. Galuzzi, A. Mirarchi, E. L. Viganò, L. De Gioia, C. Damiani, F. Arrigoni, *J. Chem. Inf. Model.* **2022**, *62*, 4748.

[57] R. Sarangi, S. Maity, A. Acharya, *J. Chem. Theory Comput.* **2024**, *20*, 6747.

[58] R. Fedorov, G. Gryn'ova, *J. Chem. Theory Comput.* **2023**, *19*, 4796.

ChemPhysChem

Research Article
doi.org/10.1002/cphc.202401098

Chemistry Europe
European Chemical
Societies Publishing

[59] Z. Si, D. Liu, W. Nie, J. Hu, C. Wang, T. Jiang, H. Yu, Y. Fu, *J. Chem. Inf. Model.* **2024**.

[60] L. Jia, É. Brémond, L. Zaida, B. Gaüzère, V. Tognetti, L. Joubert, *J. Comput. Chem.* **2024**, *45*, 2383.

[61] E. Kraka, W. Zou, Y. Tao, *WIREs Comput. Mol. Sci.* **2020**, *10*, 1480.

[62] E. Kraka, M. Quintano, H. W. La Force, J. J. Antonio, M. Freindorf, *J. Phys. Chem. A* **2022**, *126*, 8781.

[63] L. Banci, *J. Biotechnol.* **1997**, *53*, 253.

[64] A. Merlino, A. Vergara, F. Sica, L. Mazzarella, *Marine Genomics* **2009**, *2*, 51.

[65] F. Walker, *Chem. Rev.* **2004**, *104*, 589.

[66] S. Zaric, D. Popovic, E. Knapp, *Biochemistry* **2001**, *40*, 7914.

[67] P. P. Samuel, D. A. Case, *Biochemistry* **2020**, *59*, 4093.

[68] S. Abbruzzetti, A. J. Barker, I. Villar, C. Pérez-Rontomé, S. Bruno, G. Cerullo, C. Viappiani, M. Becana, *Int. J. Mol. Sci.* **2021**, *22*.

[69] A. De Petris, B. Chiavarino, M. E. Crestoni, C. Coletti, N. Re, S. Fornarini, *J. Phys. Chem. B* **2015**, *119*, 1919.

[70] J. D. Kelley, J. J. Leventhal, *Problems in Classical and Quantum Mechanics: Normal Modes and Coordinates*, Springer **2017**.

[71] S. Califano, *Vibrational States*, Wiley, London **1976**.

[72] E. B. Wilson, J. C. Decius, P. C. M. Cross, *Molecular Vibrations. The Theory of Infrared and Raman Vibrational Spectra*, McGraw-Hill, New York **1955**.

[73] E. B. Wilson, *J. Chem. Phys.* **1941**, *9*, 76.

[74] Z. Konkoli, D. Cremer, *Int. J. Quantum Chem.* **1998**, *67*, 1.

[75] Z. Konkoli, J. A. Larsson, D. Cremer, *Int. J. Quantum Chem.* **1998**, *67*, 11.

[76] V. Barone, S. Alessandrini, M. Biczysko, J. R. Cheeseman, D. C. Clary, A. B. McCoy, R. J. DiRisio, F. Neese, M. Melosso, C. Puzzarini, *Nat. Rev. Met. Prim.* **2021**, *1*, 38.

[77] W. Zou, D. Cremer, *Theor. Chem. Acc.* **2014**, *133*, 1451.

[78] M. Freindorf, E. Kraka, *J. Mol. Model.* **2020**, *26*, 281.

[79] M. Freindorf, A. A. A. Delgado, E. Kraka, *J. Comb. Chem.* **2022**, *43*, 1725.

[80] A. Madushanka, N. Verma, M. Freindorf, E. Kraka, *Int. J. Mol. Sci.* **2022**, *23*, 12310.

[81] R. T. Moura Jr., M. Quintano, J. J. Antonio, M. Freindorf, E. Kraka, *J. Phys. Chem. A* **2022**, *126*, 9313.

[82] J. J. Antonio, E. Kraka, *Biochemistry* **2023**, *62*, 2325.

[83] M. Freindorf, J. Antonio, E. Kraka, *J. Phys. Chem. A* **2023**, *127*, 8316.

[84] M. Freindorf, J. Antonio, E. Kraka, *J. Comput. Chem.* **2024**, *45*, 574.

[85] Y. Dangat, M. Freindorf, E. Kraka, *J. Am. Chem. Soc.* **2024**, *146*, 145, 10.1021/jacs.3c06397.

[86] Z. Konkoli, D. Cremer, *Int. J. Quantum Chem.* **1998**, *67*, 29.

[87] Z. Konkoli, J. A. Larsson, D. Cremer, *Int. J. Quantum Chem.* **1998**, *67*, 41.

[88] N. Verma, Y. Tao, W. Zou, X. Chen, X. Chen, M. Freindorf, E. Kraka, *Sensors* **2020**, *20*, 2358.

[89] M. Quintano, A. A. A. Delgado, R. T. Moura Jr, M. Freindorf, E. Kraka, *Electron. Struct.* **2022**, *4*, 044005.

[90] M. Quintano, R. T. Moura Jr, E. Kraka, *Chem. Phys. Lett.* **2024**, *849*, 141416.

[91] K. Nienhaus, S. Lutz, M. Meuwly, G. U. Nienhaus, *ChemPhysChem* **2010**, *11*, 119.

[92] M. Rizzi, J. B. Wittenberg, A. Coda, P. Ascenzi, M. Bolognesi, *J. Mol. Biol.* **1996**, *258*, 1.

[93] W. Zou, D. Cremer, *Chem. Eur. J.* **2016**, *22*, 4087.

[94] D. Cremer, E. Kraka, *Curr. Org. Chem.* **2010**, *14*, 1524.

[95] E. Kraka, J. A. Larsson, D. Cremer, Generalization of the Badger Rule Based on the Use of Adiabatic Vibrational Modes, in J. Grunenberg (Editor), *Computational Spectroscopy*, pages 105–149, Wiley, New York **2010**.

[96] I. Mayer, *Chem. Phys. Lett.* **1983**, *97*, 270.

[97] I. Mayer, *Int. J. Quantum Chem.* **1986**, *29*, 477.

[98] I. Mayer, *J. Comput. Chem.* **2007**, *28*, 204.

[99] E. Kraka, M. Freindorf, Chemical Bonding in Homogenous Catalysis – Seen Through the Eyes of Vibrational Spectroscopy, in *Reference Module in Chemistry, Molecular Sciences and Chemical Engineering – Comprehensive Computational Chemistry*, pages 1–27, Elsevier, Heidelberg **2022**.

[100] R. F. W. Bader, *Monatsh. Chem.* **2005**, *136*, 819.

[101] R. F. W. Bader, *Atoms in Molecules: A Quantum Theory (International Series of Monographs on Chemistry)*, Clarendon Press **1994**.

[102] R. F. W. Bader, *Chem. Rev.* **1991**, *91*, 893.

[103] D. Cremer, E. Kraka, *Angew. Chem. Int. Ed.* **1984**, *23*, 627.

[104] D. Cremer, E. Kraka, *Croat. Chem. Acta* **1984**, *57*, 1259.

[105] A. E. Reed, L. A. Curtiss, F. Weinhold, *Chem. Rev.* **1988**, *88*, 899.

[106] F. Weinhold, C. R. Landis, E. D. Glendening, *Int. Rev. Phys. Chem.* **2016**, *35*, 399.

[107] V. Guallar, F. H. Wallrapp, *Biophys. Chem.* **2010**, *149*, 1.

[108] C. E. Tzeliou, M. A. Mermigki, D. Tzeli, *Molecules* **2022**, *27*, e2660.1.

[109] D. A. Case, I. Y. Ben-Shalom, S. R. Brozell, D. S. Cerutti, T. E. Cheatham, V. W. D. Cruzeiro, T. A. Darden, R. E. Duke, D. Ghoreishi, M. K. Gilson, H. Gohlke, A. W. Goetz, D. Greene, R. Harris, N. Homeyer, S. Izadi, A. Kovalenko, T. Kurtzman, T. S. Lee, S. LeGrand, P. Li, C. Lin, J. Liu, T. Luchko, R. Luo, D. J. Mermelstein, K. M. Merz, Y. Miao, G. Monard, C. Nguyen, H. Nguyen, I. Omelyan, A. Onufriev, F. Pan, R. Qi, D. R. Roe, A. Roitberg, C. Sagui, S. Schott-Verdugo, J. Shen, C. L. Simmerling, J. Smith, R. Salomon-Ferrer, J. Swails, R. C. Walker, J. Wang, H. Wei, R. M. Wolf, X. Wu, L. Xiao, D. M. York, P. A. Kollman, *AMBER*, University of California, San Francisco **2018**.

[110] W. L. Jorgensen, J. Chandrasekhar, J. D. Madura, R. W. Impey, M. L. Klein, *J. Chem. Phys.* **1983**, *79*, 926.

[111] C. Adamo, V. Barone, *J. Chem. Phys.* **1999**, *110*, 6158.

[112] R. Ditchfield, W. J. Hehre, J. A. Pople, *J. Chem. Phys.* **1971**, *54*, 724.

[113] L. W. Chung, W. M. C. Sameera, R. Ramozzi, A. J. Page, M. Hatanaka, G. P. Petrova, T. V. Harris, X. Li, Z. Ke, F. Liu, H.-B. Li, L. Ding, K. Morokuma, *Chem. Rev.* **2015**, *115*, 5678.

[114] S. Zhao, Z.-H. Li, W.-N. Wang, Z.-P. Liu, K.-N. Fan, Y. Xie, H. F. Schaefer, *J. Chem. Phys.* **2006**, *124*, 184102.

[115] C. J. Cramer, D. G. Truhlar, *Phys. Chem. Chem. Phys.* **2009**, *11*, 10757.

[116] S. Li, J. M. Hennigan, D. A. Dixon, K. A. Peterson, *J. Phys. Chem. A* **2009**, *113*, 7861.

[117] M. K. Safo, G. P. Gupta, F. A. Walker, W. R. Scheidt, *J. Am. Chem. Soc.* **1991**, *113*, 5497.

[118] M. J. Frisch, G. W. Trucks, H. B. Schlegel, G. E. Scuseria, M. A. Robb, J. R. Cheeseman, G. Scalmani, V. Barone, G. A. Petersson, H. Nakatsuji, X. Li, M. Caricato, A. V. Marenich, J. Bloino, B. G. Janesko, R. Gomperts, B. Mennucci, H. P. Hratchian, J. V. Ortiz, A. F. Izmaylov, J. L. Sonnenberg, D. Williams-Young, F. Ding, F. Lipparini, F. Egidi, J. Goings, B. Peng, A. Petrone, T. Henderson, D. Ranasinghe, V. G. Zakrzewski, J. Gao, N. Rega, G. Zheng, W. Liang, M. Hada, M. Ehara, K. Toyota, R. Fukuda, J. Hasegawa, M. Ishida, T. Nakajima, Y. Honda, O. Kitao, H. Nakai, T. Vreven, K. Throssell, J. A. Montgomery Jr, J. E. Peralta, F. Ogliaro, M. J. Bearpark, J. J. Heyd, E. N. Brothers, K. N. Kudin, V. N. Staroverov, T. A. Keith, R. Kobayashi, J. Normand, K. Raghavachari, A. P. Rendell, J. C. Burant, S. S. Iyengar, J. Tomasi, M. Cossi, J. M. Millam, M. Klene, C. Adamo, R. Cammi, J. W. Ochterski, R. L. Martin, K. Morokuma, O. Farkas, J. B. Foresman, D. J. Fox, Gaussian 16, Gaussian Inc. Wallingford CT **2016**.

[119] W. Zou, R. Moura Jr., M. Quintano, F. Bodo, Y. Tao, M. Freindorf, M. Z. Makoś, N. Verma, D. Cremer, E. Kraka, LModeA2023, Computational and Theoretical Chemistry Group (CATCO), Southern Methodist University: Dallas, TX, USA **2023**.

[120] T. A. Keith, AIMALL, TK Gristmill Software, Overland Park KS **2017**.

[121] D. Setiawan, D. Sethio, D. Cremer, E. Kraka, *Phys. Chem. Chem. Phys.* **2018**, *20*, 23913.

[122] E. Kraka, D. Cremer, *Rev. Proc. Quim.* **2012**, pages 39–42.

[123] M. Kaupp, D. Danovich, S. Shaik, *Coord. Chem. Rev.* **2017**, *344*, 355.

[124] J. J. Antonio, E. Kraka, *Phys. Chem. Chem. Phys.* **2024**, *26*, 15143.

[125] B. M. T. C. Peluzo, M. Z. Makoś, R. T. Moura Jr, M. Freindorf, E. Kraka, *Inorg. Chem.* **2023**, *62*, 12510.